# Appendix

## Unraveling the hierarchical structure of saturated monoacid triglycerides during crystallization: A comprehensive time-resolved X-ray Scattering study

### Appendix 1. Long spacing transitions

*This appendix addresses the repeatability of the SAXS experiment for the 30%FHRO dilution in HOSO. The analysis was repeated in a Xeuss 3.0 XRS system (Xenocs, Grenoble, France) with an Eiger2R 1M detector (Dectris, Baden, Switzerland). A Cu-source (Genix 3D, Xenocs, Grenoble, France) generated the X-ray beam at a wavelength of 1.54 Å, operating at 50 kV and 0.60 mA. The sample was placed in a quartz capillary and sealed with wax. The capillary was then placed in a THMS600 Linkam stage and the time-temperature profile was replicated (melt for 15 minutes at 80°C, cooling at 10°C/min to 15°C). The isothermal time was extended from 15 minutes to 8 hours 30 minutes. Measurements were taken each 60 s for the first 20 minutes (exposure time = 60 s). After that, one acquisition was taken every 20 minutes (exposure time = 600 s). Only SAXS profiles were acquired, using a sample to detector distance of 360 mm. The final profile was corrected for background scattering, and the signal from the empty capillary was subtracted using XSACT software (Xenocs). Results are shown in* Figure 1.

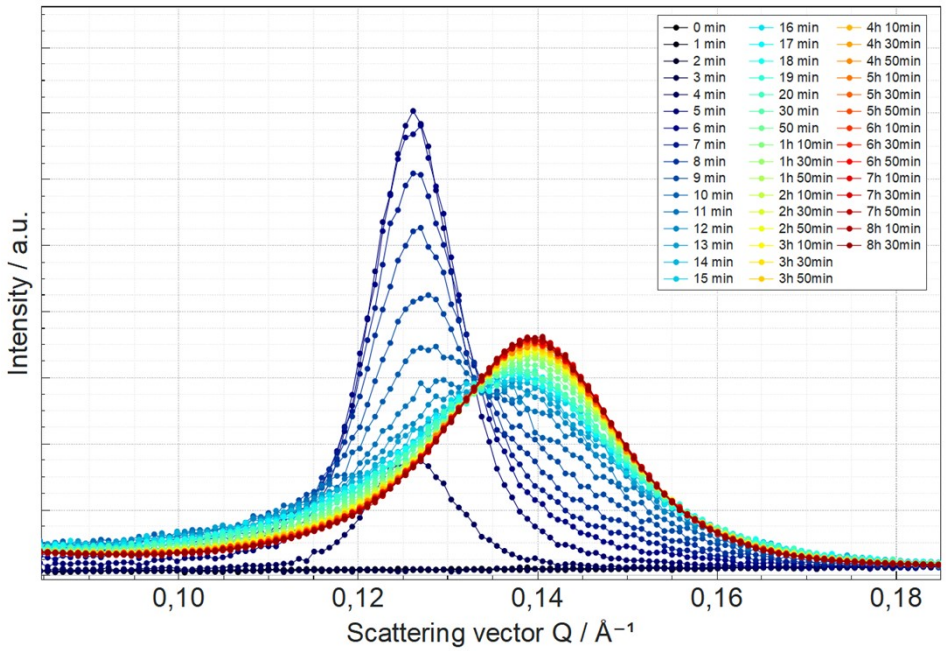


Figure 1. Small Angle X-ray scattering results for a 30% dilution of FHRO in HOSO. The sample was crystallized from 80°C to 15°C at 10°C/min. The sample was then allowed to crystallize isothermally for 8 hours and 30 minutes. The resulting profile indicates that long spacing modifications take long periods of time.

Results indicate that the transformation from a 2L(α) to a 2L(β) structure occurs over an extended period. Although a peak indicative of a 2L(β) arrangement, suggesting the formation of an angle of tilt, appears at 30 minutes of crystallization, the system continues to evolve throughout the entire measurement period of 8 hours and 30 minutes.

## Appendix 2. Comparative Analysis of Methods for Determining CNP Thickness

This appendix addresses the various methods used to measure CNP thickness and critically discusses their shortcomings. We have described three main methods for determining CNP thickness: (1) the Scherrer equation, (2) USAXS modeling and (3) the BWA method. As outlined in the main text, although the overall behavior remains consistent, deviations in the absolute values between methods are evident. Each method relies on a specific part of the scattering curve, and as these curves evolve over time, certain methods may capture the transformations more effectively than others. This issue is particularly relevant for the stearic sample, where the largest discrepancies between methods are observed (see Figure 7F in the main text).

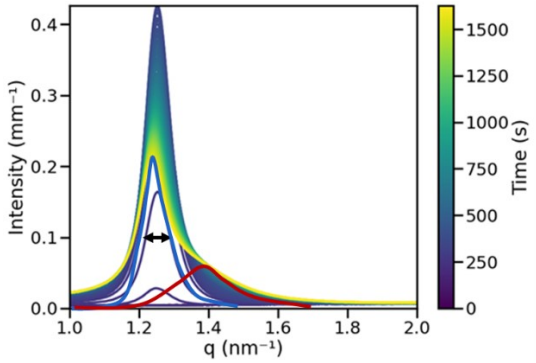


*Figure 2. Diagram illustrating how the FWHM accounts for only a single peak. Although a secondary peak is emerging at higher q-values (indicated in red), unless this new peak is sufficiently developed, the FWHM will only consider the highest peak (indicated in blue). As a result, the Scherrer equation does not account for the secondary part of the curve, leading to an overestimation of the CNP size.*

*First, the Scherrer equation uses the FWHM of the 001 SAXS peak.[1] As seen in Figure 2, a secondary peak is beginning to emerge at higher q-values. However, since the FWHM criterion typically focuses on the highest peak, the Scherrer equation overlooks this secondary feature. Consequently, the presence of a secondary distribution, indicating a reduction in the size of CNPs, does not affect the final size estimation. Therefore, it is evident that the Scherrer equation tends to overestimate the average CNP size. As such, this highlights the importance of considering multiple peaks and broader features when using Scherrer analysis for more accurate size determinations of CNPs.*

Furthermore, Penagos et al. (2024) introduced a model applicable to the USAXS range for determining CNP thickness [2]. This model utilizes the curvature of the Guinier bend in the USAXS profile to estimate thickness. When a transition between two distributions occurs (*Figure 3*), two bends simultaneously emerge. This results in an overall increase in system polydispersity, as observed in the bimodal thickness distribution in the BWA section, which diminishes the curvature of the bend. Consequently, whenever used during phase transitions, the model may struggle to identify a distinct bend to fit, leading to an underestimation of the CNP size.

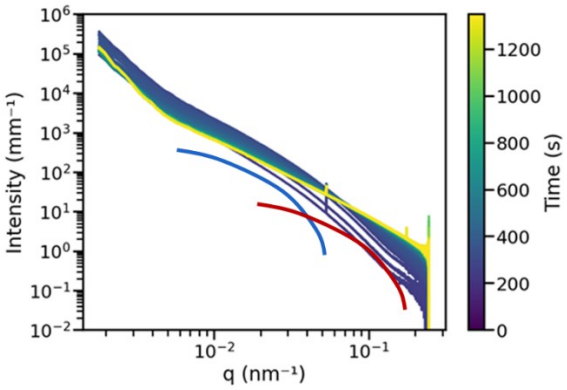


*Figure 3. Diagram illustrating how curvature is lost when two bumps merge, resulting in a straight line. This phenomenon occurs when a transition between two distributions happens, leading to two bends emerging simultaneously in the scattering profile. The increased polydispersity reduces the curvature of the bend, making it more challenging to identify distinct bends and potentially leading to an underestimation of the CNP size.*

Finally, the BWA method can be used to estimate the average weighted number of lamellae per CNP found in the crystallite thickness distribution.[3, 4] This method utilizes a Fourier transformation-based methodology to obtain a frequency distribution from a function that describes the entirety of the 001 SAXS reflection. In this case, a large number of gaussian terms (25) were utilized to avoid oversimplification of the SAXS curve and to avoid presumptions about the shape of the distributions (see *Figure 4*) [2, 5, 6]. In this case, the transformations on the SAXS area are well captured by the BWA method, and thus, it is considered to be the best available method at estimating CNP thickness values.

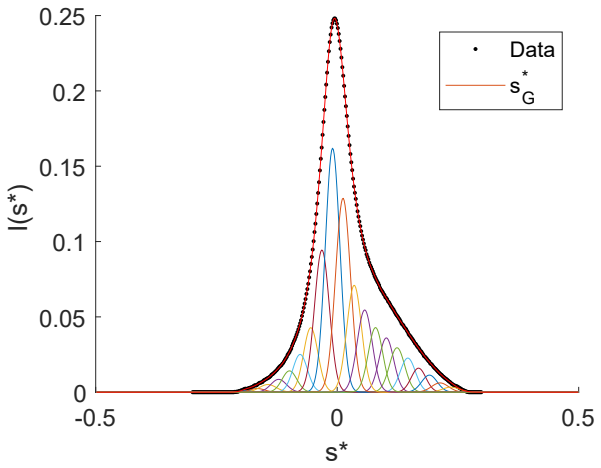


*Figure 4. Diagram showcasing how the intensity of the 001 reflection is fitted to a sum of 25 gaussian curves in order to avoid oversimplification of the fitted data. As a result, the $S_G^*$ function takes into account the emerging distribution to the left. For more information about the meaning of S*, the reader is directed elsewhere [4].*

## Appendix 3. CNP Aggregation

This appendix aims at giving some additional information to better understand the relationship between fractality of CNP aggregates and the power law factor P. For this, first, a general discussion on fractal geometry will be presented, followed by some words on the interpretation of slope in the Porod plot.

Fractal dimensions offer a way to quantify natural objects with complex structures that traditional Euclidean geometry cannot measure.[7, 8] Fractal dimensions provide the tools to better describe disordered mass distributions, which can help us establish relationships between mass and radius. In classical Euclidean geometry, objects are defined by integer dimensions: a line is 1-dimensional, a plane is 2-dimensional, and a volume is 3-dimensional . This type of geometry is suitable for quantifying ideal, or regular objects. For instance, consider a solid 2-dimensional disk. In this Euclidean object, the mass (M) scales with the radius (r) as Equation 4.[7]

$$M(r) \sim r^2 \quad [1]$$

However, when a line or a plane is sufficiently kinked, it can create an object that lies between these dimensions, resulting in a fractional, or fractal, dimension. Fractal objects are characterized by self-similarity, meaning their patterns repeat at various scales. For a disordered mass distribution exhibiting statistical self-similarity at different scales, the mass-radius relationship follows Equation 5, where D is a fractional or fractal dimension.[7] For more information on fractal dimensions and mass distributions, the reader is referred elsewhere.[7, 8]

$$M(r) \sim r^D \quad [2]$$

Fractal dimensions can often be found via X-ray scattering. The Porod region in scattering experiments refers to the range of scattering vector q where the scattering intensity follows a specific power-law behavior. Scattering from a mass fractal can be analyzed using the 3D Fourier transform of the scattering length distribution function, which yields a power-law relationship with the fractal dimension of a sample (Equation 6).

$$I(q) \sim q^{-P} \quad [3]$$

Depending on the value of P, it is then possible to interpret the configuration of a certain system. In fact, P gives an idea of how densely the mass is distributed within a volume. Lower power law values can thus be interpreted as mass fractals, which indicate loose conformations. In contrast, as the P value increases, the system is more compact. Figure *5* presents a simplified graphical representation of the meaning of each power law (based on Hammouda [9]). The diagram here presented must be used merely as a depiction.

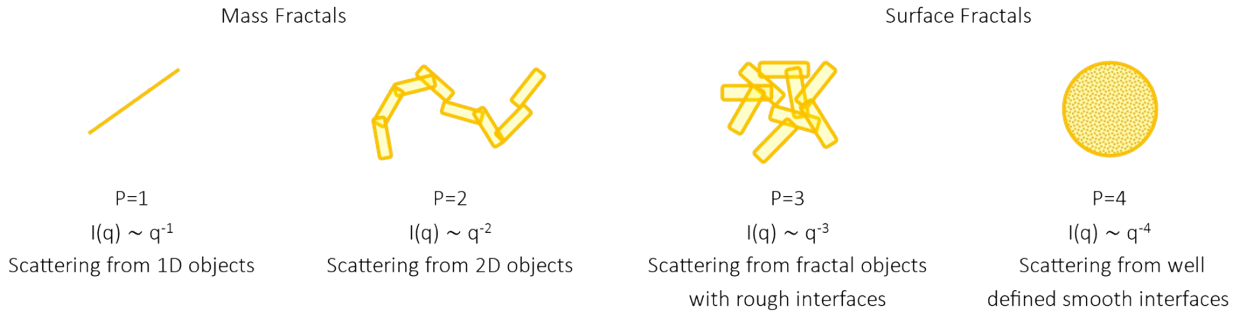


Figure 5. Graphic representation relating power law P to the overall TAG aggregation behavior. The diagram is based on illustrations presented by Hammouda [9].

Lastly, it is also important to mention the relationship between configuration and surface characteristics. In fact, in the work for Peyronel, et al. [10], Porod exponents are mostly interpreted as surface configurations. In fact, exponents between 3 and 4, are interpreted as rough interfaces whilst a value of P=4 is interpreted as smooth surfaces [11]. This interpretation is actually consistent with the interpretation presented in Figure 5. In fact, higher fractal dimensions indicate denser packing, which allows less voids and therefore smoother surfaces. In contrast, lower values suggest a more spread-out structure, which in return produces more surface roughness.

## References


1. N. C. Acevedo, in *Structure-Function Analysis of Edible Fats*, 2018, pp. 1-19.
2. I. A. Penagos, F. De Witte, T. Rimaux, W. Chèvremont, I. Pintelon, K. Dewettinck and F. Van Bockstaele, *Soft Matter*, 2024.
3. R. den Adel, K. van Malssen, J. van Duynhoven, O. O. Mykhaylyk and A. Voda, *Eur J Lipid Sci Tech*, 2018, **120**, 1800222.
4. K. Rondou, F. De Witte, T. Rimaux, W. Dewinter, K. Dewettinck, J. Verwaeren and F. Van Bockstaele, *Journal of the American Oil Chemists' Society*, 2022, **99**, 1019-1031.
5. F. De Witte, I. A. Penagos, K. Rondou, K. Moens, B. Lewille, D. A. Tzompa-Sosa, D. Van de Walle, F. Van Bockstaele, A. G. Skirtach and K. Dewettinck, *Crystals*, 2024, **14**, 142.
6. F. De Witte, I. A. Penagos, D. Van de Walle, A. G. Skirtach, K. Dewettinck and F. Van Bockstaele, *Foods*, 2024, **13**, 1372.
7. S. S. Narine and A. G. Marangoni, *Food research international*, 1999, **32**, 227-248.
8. P. Meakin, *Advances in Colloid and Interface science*, 1987, **28**, 249-331.
9. B. Hammouda, 2008.
10. F. Peyronel, J. Ilavsky, G. Mazzanti, A. G. Marangoni and D. A. Pink, *Journal of Applied Physics*, 2013, **114**.
11. F. Peyronel and D. A. Pink, in *Structure-Function Analysis of Edible Fats*, 2018, pp. 267-285.